
Hyperspectral Image segmentation and its application in abdominal surgery

Hamed Akbari* and Yukio Kosugi

Department of Mechano-Micro Engineering,
Tokyo Institute of Technology,
G2-16, 4259 Nagatsuta, Midori-ku,
Yokohama 226-8502, Japan
Fax: +81-45-924-5172
E-mail: akbari.h.aa@m.titech.ac.jp
E-mail: kosugi@pms.titech.ac.jp
*Corresponding author

Kazuyuki Kojima

Gastrointestinal Surgery Department,
Tokyo Medical and Dental University,
1-5-45 Yushima, Bunkyo-ku,
Tokyo 113-8519, Japan
Fax: +81-3-5803-0139
E-mail: k-kojima.srg2@tmd.ac.jp

Naofumi Tanaka

Operation Center University Hospital of Medicine,
Tokyo Medical and Dental University,
1-5-45, Yushima, Bunkyo-ku,
Tokyo 113-8519, Japan
Fax: +81-3-5803-0171
E-mail: tanaka.oper@tmd.ac.jp

Abstract: The anatomical variations and unpredictable nature of surgeries make the visibility very important, especially to correctly diagnose problems intraoperatively. In this paper, hyperspectral imaging is proposed as a visual supporting tool to detect different organs and tissues during surgeries. This technique can aid the surgeon to find ectopic tissues and to diagnose tissue abnormalities. Two cameras were used to capture images within 400–1700 nm spectral range. The high-dimensional data were classified using a Support Vector Machine (SVM). This method was evaluated for the detection of the spleen, colon, small intestine, urinary bladder and peritoneum in abdominal surgeries on pigs.

Keywords: hyperspectral image segmentation; abdominal organ segmentation; HSI; hyperspectral image; medical imaging; tissue detection; spectrophotometry.

Reference to this paper should be made as follows: Akbari, H., Kosugi, Y., Kojima, K. and Tanaka, N. (2009) 'Hyperspectral Image segmentation and its application in abdominal surgery', *Int. J. Functional Informatics and Personalised Medicine*, Vol. 2, No. 2, pp.201–216.

Biographical notes: Hamed Akbari received his MD from the Tehran University of Medical Science in 2000, an MSc in Biomechanical Engineering in 2004 and a PhD in Biomedical Engineering from the Tokyo Institute of Technology in 2008. He has worked for more than two years as a clinician and also has teaching experience at Kar University in Tehran. Since October 2008, he has been working as a postdoctoral fellow at the Tokyo Institute of Technology. His field of research is medical signal and image processing.

Yukio Kosugi received MS and Dr. Eng. Degrees from the Tokyo Institute of Technology in 1972 and 1975, respectively, both in electronics. He is currently a professor at the Interdisciplinary Graduate School of Science and Engineering, the Tokyo Institute of Technology. His research interests include information processing in the nervous system and neural-network-aided image processing in medical and remote sensing fields.

Kazuyuki Kojima received his MD from Gunma University in 1987. He is currently a Professor in the Gastrointestinal Surgery Department, Tokyo Medical and Dental University. His research interests include the objective estimation of less-invasive laparoscopic surgery and the influence of laparoscopic devices on nerves.

Naofumi Tanaka graduated from the Shinshu University School of Medicine in 1990. He has worked as an anaesthesiologist in the Tokyo Medical and Dental University (TMDU) since 1990. From 1992 to 1995, he worked as an anaesthesiologist at the Tokyo Metropolitan Fuchu hospital. Since 1995, he has been working in an operation centre at TMDU. He received a Master's Degree, a "Master of medical administration" (TMDU), in 2005 and received a PhD in Medicine degree (TMDU) in anaesthesiology at the same time. He is now a lecturer in and director of the operation centre of the university hospital's faculty of medicine. His study areas are anaesthesiology, operative medicine and the collaborations among medicine, dentistry and engineering.

1 Introduction

Different imaging techniques such as Magnetic Resonance Imaging (MRI), Computed Tomography (CT), ultrasonography, nuclear imaging and Doppler scanning have radically developed modern biomedical imaging. One of the most challenging fields in medical imaging is image segmentation because of the ambiguity between the organ and its adjacent tissues. This problem becomes more difficult in dynamic situations such as in live or moving subjects, since the movements of the organ will worsen the detection (Liu et al., 2007). This problem becomes more challenging in special situations like anatomic variations, ectopic tissues and tissue abnormalities.

Hyperspectral Image (HAI) data provide a powerful tool for non-invasive tissue analyses. This technology is capable of capturing both the spatial and the spectral information of an organ in one snapshot. In fact, the imaging system produces several narrow band images at different wavelengths. Compared with conventional colour

cameras and other filter-based imaging systems, this system produces full neighbouring spectral data with spectral and spatial information (Akbari et al., 2008a).

HSI can extend the human vision to near-infrared and infrared wavelength regions. This imaging technology has been modified from a complicated technique in satellite or aircraft systems to a compact tool in imaging and spectroscopy that can be utilised in medicine. Hyperspectral imaging has already been applied in the medical field. HSI is applied to provide quantitative data about the tissue oxygen saturation in patients with peripheral vascular disease (Kellicut et al., 2004), to detect ischaemic regions of the intestine during surgery (Akbari et al., 2008b), to predict and follow healing in foot ulcers of diabetic patients (Khaodhiar et al., 2007), to diagnose haemorrhagic shock (Cancio et al., 2006), to detect chronic mesenteric ischaemia during endoscopy (Friedland et al., 2007) and to detect skin cancer in mice (Martin et al., 2006).

Hyperspectral imaging provides reliable information in near real-time with a convenient device for the surgeon in the operating room. It has a greater sensitivity for detecting a residual tumour tissue than current surgical tissue sampling techniques (Freeman et al., 2005). This technique is used as a visual support tool to enhance the regions covered with a layer of blood during surgeries (Monteiro et al., 2006). A hyperspectral imaging endoscope is used for the early detection of dysplasia and cancer in lung epithelia (Lindsley et al., 2004). Recently, a near-infrared hyperspectral imaging system has been coupled with a conventional surgical laparoscope for minimally invasive surgical procedures, specifically to help guide laparoscopic surgeons to visualise biliary anatomy (Zuzak et al., 2007).

So far, none of the research has used near-infrared or infrared wavelengths for intra-abdominal organ segmentation. Nevertheless, spectral measurement in the field of surgery has appealing advantages. For instance, the measurement can be done without physical contact, many points can be measured simultaneously, and it can be performed without disrupting the procedure. Surgeons can survey and examine a vast area less invasively without actually removing the tissue. In this research, a database of spectral signatures for abdominal organs was created using two hyperspectral cameras (400–1000 nm and 900–1700 nm). Using these signatures, the abdominal view through a large incision was segmented. This technique can be useful for finding ectopic tissues and for the diagnosis of tissue abnormalities, particularly those that were not predicted. The surgical hyperspectral data were captured during surgeries on two pigs.

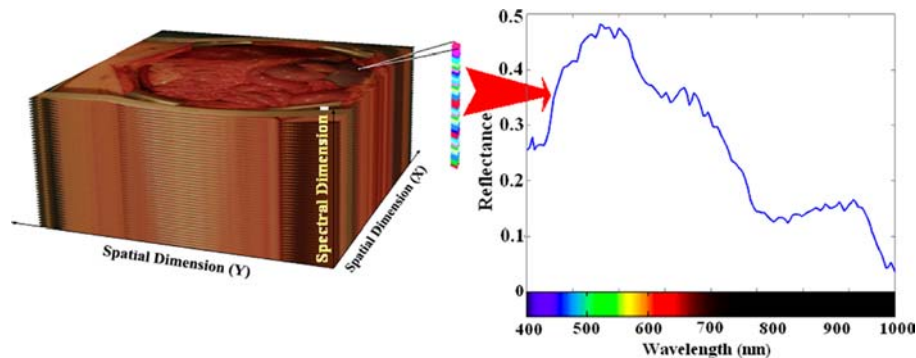
Recently, SVMs have been increasingly used in multispectral and HIS. This research, applying SVMs to HSI classification, has shown superior performance to the other available classification methods (Camps-Valls and Bruzzone, 2005; Camps-Valls et al., 2004; Melgani and Bruzzone, 2004; Huang et al., 2002; Brown et al., 2000). An SVM was used in the current study for image segmentation.

2 Materials and methods

To capture the HSI data, two cameras, an ImSpector N17E and a V10E, manufactured by Spectral Imaging Ltd., Oulu, Finland, were used. The ImSpector is a direct sight imaging spectrograph that can be quickly combined with a broad range of industrial and scientific monochrome area cameras to form a spectral camera. Each pixel in the HSI has a sequence of reflectance in different spectral wavelengths that can display the spectral signature of that pixel. Figure 1 shows a schematic view of the HSI. Since there are a

large number of data for each image, an SVM was used to segment the image. After this step, the majority of pixels were detected, although there were some pixels that were lost due to glare. Most of these pixels were located at the mid-portion of the organs. To solve this problem, we have applied an image fill function and region growing in the post-processing steps. The technique was evaluated during the abdominal surgeries on two pigs under general anaesthesia.

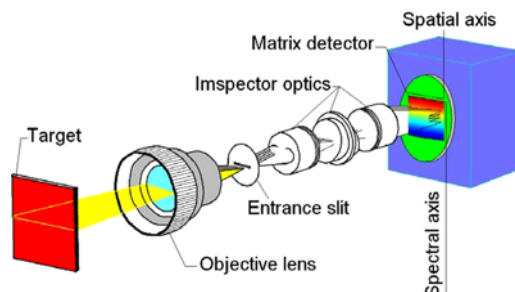
Figure 1 On the left, a schematic view of a Hyperspectral Image of a pig's abdomen is shown. On the right, the spectral graph of one pixel from the urinary bladder is shown. The graph depicts the reflectance for each pixel in that wavelength (see online version for colours)



2.1 Hyperspectral cameras

The main components of the hyperspectral camera are shown in Figure 2. The light source, i.e., the halogen lamps, illuminate the object to be captured, and the camera's objective lens collects the radiation from the object and displays an image on the entrance slit plane. The slit determines the field of imaging in spatial directions. The radiation from the slit is projected to the ImSpector optics, the Prism-Grating-Prism (PGP) components; therefore, the direction of propagation of the radiation changes depending on its wavelength. Then, it is focused on the matrix detector. Every object's point is represented on the matrix detector by a series of monochromatic points that makes a continuous spectrum in the direction of the spectral axis.

Figure 2 Design of the ImSpector hyperspectral imaging sensor (Specim Spectral Imaging Ltd.) (see online version for colours)



The capturing technique of the camera is a pushbroom scanner type of imaging spectrometer in which the entrance slit limits the imaging field. This technique allows the 2D detector matrix to capture the spectral dimension and one spatial dimension in one snapshot. The second spatial dimension is generated by scanning the object. By moving the camera's field of view relative to the object, the second spatial dimension is created.

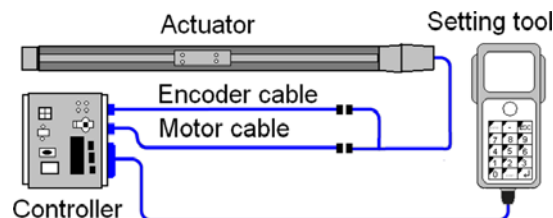
The PGP component is composed of a special grating between two prisms. Short and long pass filters are usually placed between the grating and the prisms, eliminating unwanted wavebands and changing the spectral response. Since the filters are incorporated in this technique inside a PGP, the reflections from their surfaces can be eliminated. The PGP contains the aperture stop of the spectrograph optics that is set in contact with the grating. Unlike a direct vision prism where the dispersion is a non-linear small dispersion, the diffraction grating in the PGP supplies a large linear dispersion (Aikio, 2001).

Two cameras, the ImSpector N17E and the V10E, capture the wavelength in the range of 400–1700 nm. The V10E model has the spectral range of 400–1000 nm, a dispersion of 97.5 nm/mm and a spectral resolution of 5 nm (with a 30 μ m slit). The N17E model has a spectral range of 900–1700 nm, a dispersion of 110 nm/mm and a spectral resolution of 5 nm (with a 30 μ m slit). Different wavelengths will be transmitted for only the small region of the object that is exactly in front of the entrance slit. By shifting the camera between subsequent images, ultimately all parts of the object and all corresponding wavelengths are captured. Therefore, for each wavelength, a monochromatic spectral image can be constructed from the HSI set.

2.2 Hyperspectral Image capturing

The second spatial dimension is generated by scanning the object. By moving the camera's field of view relative to the object, the second spatial dimension is created. The linear actuator, a ROBO Cylinder Slider, model RCS-SM-A-100-H-1000-T1-S, is used to move the camera. This actuator is controlled by an XSEL-J-1-100A-N3-EEE-2-1 type controller. The actuator and controller are manufactured by IAI Corporation, Japan. The actuator works with a ball screw drive system, a 100 W motor and an absolute incremental encoder. The actuator has an 84.9 N rated thrust, a 1–1000 mm/s speed, a ± 0.02 mm positioning repeatability and a maximum backlash of 0.05 mm. The actuator is connected to the controller by two cables: the encoder cable and the motor cable. The movement and velocity are adjusted by a setting tool that is connected to the controller. The actuator moves the camera with a constant velocity. Figure 3 shows the linear actuator set-up.

Figure 3 The linear actuator set-up (see online version for colours)



The experimental data acquisition set-up consists of a pair of 500 W halogen lamps with diffusing reflectors as the light sources and the computer-controlled linear actuator that is fixed on a bridge. Figure 4 shows the acquisition set-up. The two sources provide a fairly uniform illumination of the subject. Also, the camera has been calibrated and fixed on the frame. The distance between the lens and the abdomen is constant.

Figure 4 The acquisition set-up (see online version for colours)



2.3 Data normalisation

To address the problem of the spectral non-uniformity of the illumination device and the influence of the dark current, the radiance data were normalised to yield the radiance of the specimen. To perform this pre-processing step, the radiance of a standard reference white board placed in the scene and the dark current were measured by keeping the camera shutter closed. Then, the raw data were corrected to reflectance using the following equation:

$$R(\lambda) = \frac{I_{\text{raw}}(\lambda) - I_{\text{dark}}(\lambda)}{I_{\text{white}}(\lambda) - I_{\text{dark}}(\lambda)} \quad (1)$$

where $R(\lambda)$ is the calculated reflectance value for each wavelength, $I_{\text{raw}}(\lambda)$ is the raw data radiance value of a given pixel, and $I_{\text{dark}}(\lambda)$ and $I_{\text{white}}(\lambda)$ are, respectively, the dark current and the white board radiance acquired for each line and spectral band of the sensor. The dark current in the ImSpector N17E camera was captured and included in the main *.raw data file. However, in the ImSpector V10E, it was captured in a separate file in *.drk format. The white reference board should be placed in the capturing field when the ImSpector V10E is used. However, the white reference should be captured separately when the ImSpector N17E is used.

2.4 Normalised Difference Indexes

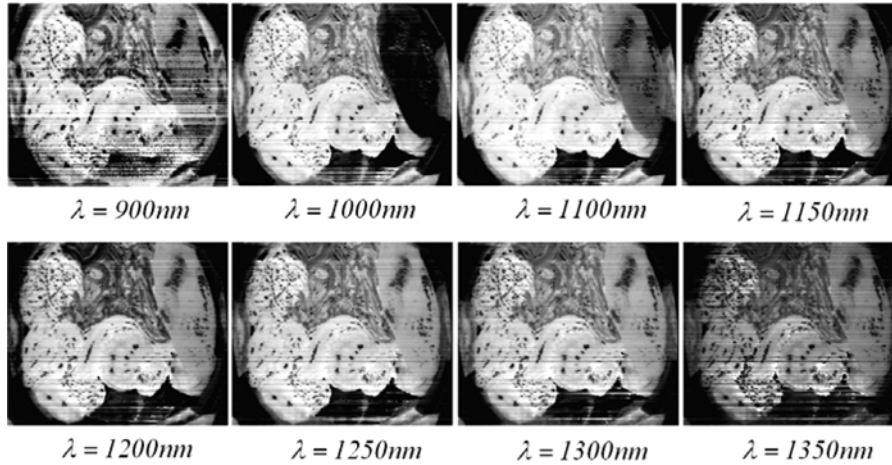
The Normalised Difference Index (NDI) is one of the simplest methods to evaluate hyperspectral data. A large number of data can be visualised by this method in a real-time manner. This technique has been used in different research studies to estimate chlorophyll content (Richardson et al., 2002), to evaluate the effects of nitrogen fertilisation treatments (Moran et al., 2000), to estimate water content (Datt et al., 2003), and to estimate the yields of salt- and water-stressed forages (Poss et al., 2006).

The camera captures a sequence of images in different spectral bands. To find the appropriate NDI, different wavelengths were evaluated. A few wavelengths were selected to enhance the difference of organs or tissues. Using these NDIs, it is possible to enhance the contrasts among the organs in different wavelengths. The following equation is applied to calculate the NDI:

$$\text{NDI}(\lambda) = \frac{I(\lambda) - I(\lambda = 1550)}{I(\lambda) + I(\lambda = 1550)} \quad (2)$$

where $\text{NDI}(\lambda)$ is the normalised difference index in the wavelength λ and $I(\lambda)$ is the intensity of a given pixel in the wavelength λ . Figure 5 shows the NDI images in the selected sample wavelengths. For instance, for a wavelength of 1000 nm, the NDI of the spleen is the lowest among the organs. The NDI (1200 nm) displays a good contrast for the peritoneum. Although this technique is a fast method for visualisation, it does not result in precise segmentation in the image processing. Therefore, for the image segmentation in this paper, all the wavelengths were processed by the SVM.

Figure 5 Eight sample images using the proposed NDI at different wavelengths



2.5 Artificial neural networks

A successful approach to hyperspectral data classification is based on the use of Multilayer Perceptron (MLP) artificial neural networks and Radial Basis Function Neural Networks (RBFNNs). However, these approaches are not effective when dealing with a high number of spectral bands, since they are highly sensitive to the Hughes phenomenon (Hughes, 1968). In recent years, SVMs have been successfully used for hyperspectral

data classification. SVMs can efficiently handle large input spaces or noisy samples and produce sparse solutions (Camps-Valls and Bruzzone, 2005). Therefore, an SVM was chosen to classify the compressed data and to segment the HSIs.

2.5.1 Support Vector Machines (SVMs)

Support Vector Machines (SVMs) are supervised classifiers that use a small number of exemplars selected from the tutorial data set, with the intention to enhance the generalisation ability. Unlike perceptrons and Learning Vector Quantisation (LVQ) (Kohonen, 1987), the SVM has a pair of margin zones on both sides of the discriminate function. The SVM is a popular classifier based on statistical learning theory as proposed by Vapnik (1995) and Brown et al. (2000). The SVM framework is more appropriate for empirical mixture modelling, as non-separable distributions of pure classes can be handled appropriately, as well as non-linear mixture modelling (Brown et al., 2000).

The training phase of SVMs looks for a linear optimal separating hyperplane as a maximum margin classifier with respect to the training data. Since the training data are not linearly separable, the kernel method was used in our study. Kernel-based methods map data from an original input feature space to a kernel feature space of a higher dimensionality and then solve a linear problem in that space. The Least Squares SVM (LS-SVM), a modified configuration of the SVM, was used in this paper. These methods enable us to interpret and design learning algorithms geometrically in a kernel space that is non-linearly related to the input space, thus combining statistics and geometry in an effective way (Camps-Valls and Bruzzone, 2005; Liu et al., 2007).

2.5.2 Least Squares SVM (LS-SVM)

In SVMs, a convex Quadratic Programme (QP) solves the classification problem. Suykens and Vandewalle (1999) proposed a new version of SVM classifiers, named the LS-SVMs. In LS-SVMs, instead of inequality constraints, a two-norm with equality is applied. Therefore, instead of a QP problem in dual space, a set of linear equations is obtained. The SVM tries to find a large margin for classification. However, the LS-SVM that was used in this paper looks for a ridge regression for classification with binary targets. This method overcomes some disadvantages of SVMs. For example, the selection of hyperparameters is not as problematic. The size of the matrix involved in the QP problem is also directly proportional to the number of training points (Van Gestel et al., 2004).

Suykens and Vandewalle (1999) modified Vapnik's optimisation function of the SVM as follows:

$$\text{Min}_{w,b,e} f(w,e) = \frac{1}{2} w^T w + \gamma \frac{1}{2} \sum_{i=1}^N e_i^2 \quad (3)$$

subject to the equality constraints

$$y_i [w^T \phi(x_i) + b] = 1 - e_i, \quad i = 1, \dots, N \quad (4)$$

where w is the weighting vector, b is the bias term, e is for misclassifications and γ is the tuning parameter. This constrained optimisation problem can be solved by determining the saddle points in the Lagrange functional as

$$L(w, b, e; \alpha) = f(w, b, e) - \sum_{i=1}^N \alpha_i \{y_i [w^T \phi(x_i) + b] - 1 + e_i\} \quad (5)$$

where $\alpha_i \in R$ are Lagrange multipliers that can be positive or negative in the LS-SVM formulation.

In SVMs, it is possible to choose several types of kernel functions including linear, polynomial, RBF, MLP with one hidden layer and splines. The RBF kernel used in this paper was as follows:

$$K(x, x_i) = \exp\{-\|x - x_i\|_2^2 / \sigma^2\} \quad (6)$$

where σ is constant.

The accuracy of the SVM is significantly dependent on the selection of the kernel parameters. One commonly used parameter selection method for the SVM, the grid search method, was used in this study. The algorithm tries to find the largest error-decreasing path during training (Bao and Liu, 2006). Multi-class categorisation problems are represented by a set of binary classifiers. Here, we had input vectors of 157 elements in the ImSpector N17E images and 121 elements in the ImSpector V10E images, and each input vector was assigned to one of the seven classes (spleen, peritoneum, urinary bladder, small intestine, colon, skin and background). To prepare a set of input/target pairs for training, first we captured 100 pixels of data from each region in the surgical HSIs. The SVMs were applied one by one to the image for each class, and each pixel was labelled as an organ. The training data are different from the evaluation data. The training data are captured and labelled using anatomical data by a medical doctor. The times for algorithm training are 3–4 min and 2–3 min for the images captured by the N17E and the V10E cameras, respectively. The calculation time for the segmentation was 3–4 min and 2–3 min for the images captured by the N17E and the V10E cameras, respectively. The accuracies were more than 99%.

2.6 Post-processing

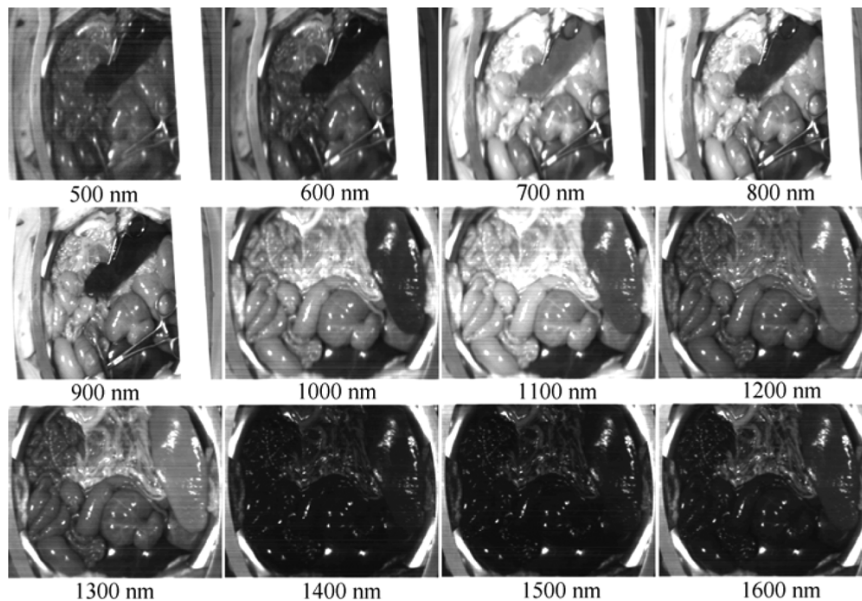
As the first step in post-processing, for detecting missed pixels that were not detected as an organ region, the image was reprocessed using the image fill function. It labels pixels that are surrounded by one organ pixel as a part of that organ. After this step, some pixels that were lost because of glare were detected. As the second step in the post-processing, to determine the boundaries of each organ, a region growing method was applied. When the boundary of a region was not labelled, this method expanded the boundary by assigning an organ pixel until it reached a neighbour pixel that was labelled as another organ. The sequence in which organ growing was carried out follows this priority string: colon, small intestine, peritoneum, spleen and urinary bladder.

3 Experimental results

The experiment was done on two pigs. The pigs underwent general anaesthesia, a large incision was created on the abdomen, and the internal organs were explored. Vital signs were evaluated during the surgery to assure constant oxygen delivery to the organs. Nine HSIs by the ImSpector N17E and seven HSIs by the ImSpector V10E were captured.

The ImSpector V10E images have 484 pixels in width, 600 pixels in length, a dispersion of 97.5 nm/mm, a spectral resolution of 5 nm (with a 30 μ m slit) and 121 band-channels between 400 nm and 1000 nm in wavelength. The ImSpector N17E images have 240 pixels in width, 370 pixels in length, a dispersion of 110 nm/mm, a spectral resolution of 5 nm (with a 30 μ m slit) and 157 wavelength bands between 900 nm and 1700 nm. The actuator velocity was set such that the resolutions of the two spatial dimensions were equal. Each HSI consisted of several narrow band images that could be displayed one by one. Figure 6 shows the images in different wavelengths that are captured using two HSIs by two cameras in a large-incision view during the abdominal surgery on the pigs.

Figure 6 Several images at different wavelengths that are captured using two Hyperspectral Images from two cameras in a large-incision view during an abdominal surgery on pigs



Each pixel of the HSIs had a series of intensities at different wavelengths. The diagrams of the intensity for the spleen, peritoneum, colon, small intestine and urinary bladder were extracted. Figure 7 shows the spectral signatures of these tissues. For each HSI, the white reference and dark current were captured separately. To change the intensity diagram to a unique spectral signature that would be reproducible and comparable, the reflectance spectra (after white calibration) were calculated. Figure 8 shows the reflectance spectra.

Figure 7 Spectral intensity signatures: the horizontal axis shows different wavelengths in nanometres, and the vertical axis shows the intensity (see online version for colours)

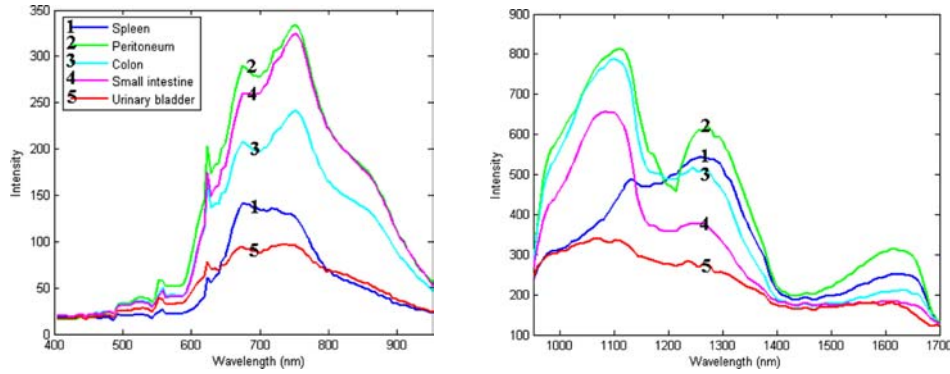
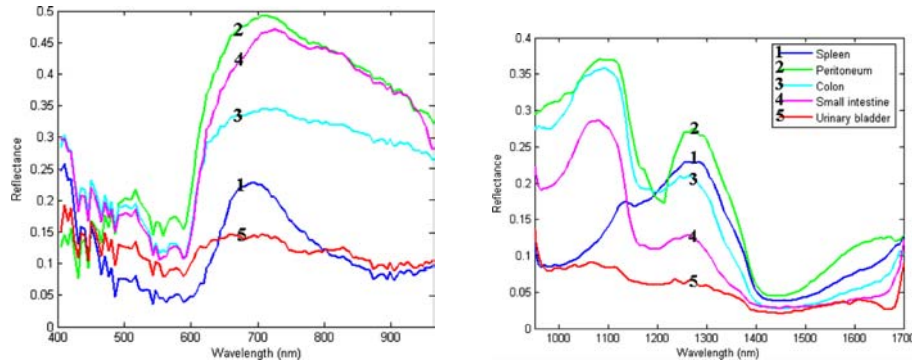


Figure 8 Reflectance spectra: the horizontal axis shows different wavelengths in nanometres, and the vertical axis shows the reflectance (see online version for colours)



The performance of the method was evaluated in nine HSIs that were captured by the ImSpector N17E and seven HSIs that were captured by the ImSpector V10E for the detection of the spleen, peritoneum, urinary bladder, small intestine and colon. Figure 9 shows a sample segmented image of the two cameras. The performance was evaluated for the quality of detection with respect to the hand-created maps by a medical doctor and by using anatomical data. The hand-created maps were used as reference maps in calculating the detection rates of our method. Performance criteria for organ or tissue detection were the False Negative Rate (FNR) and the False Positive Rate (FPR), which were calculated for each organ. When a pixel was not detected as an organ or tissue pixel, the detection was considered a false negative if the pixel was a pixel of that organ on the hand-created map. The FNR for an organ was defined as the number of false negative pixels divided by the total number of the organ pixels on the hand-created map. When a pixel was detected as an organ pixel, the detection was a false positive if the pixel was not an organ pixel on the hand-created map. The FPR was defined as the number of false positive pixels divided by the total number of non-organ pixels on the hand-created map. The pixels that were ambiguous and that the medical doctor could not label as an organ were not considered in our calculation. The numerical results of the FPR and FNR for each organ and a comparison with previously reported results (Akbari et al., 2008a) are given in Table 1.

Figure 9 Hyperspectral Images of the pig's abdomen by two cameras: (a) the RGB image corresponding to the visible and near-infrared (400–1000 nm) camera; (b) the RGB image corresponding to the invisible and near-infrared and infrared (900–1700 nm) camera; (c) the RGB image is made using three channels of the visible and near-infrared (400–1000 nm) Hyperspectral Image; (d) the RGB image is made using three channels of the invisible and near-infrared and infrared (900–1700 nm) Hyperspectral Image; (e) the segmented image of the visible and near-infrared (400–1000 nm) Hyperspectral Image using the proposed method (f) the segmented image of the invisible and near-infrared and infrared (900–1700 nm) Hyperspectral Image. Spleen is shown in red (number 1), peritoneum in cyan (number 2), colon in brown (number 3), small intestine in yellow (number 4), urinary bladder in olive (number 5), and skin in orange (number 6) (see online version for colours)

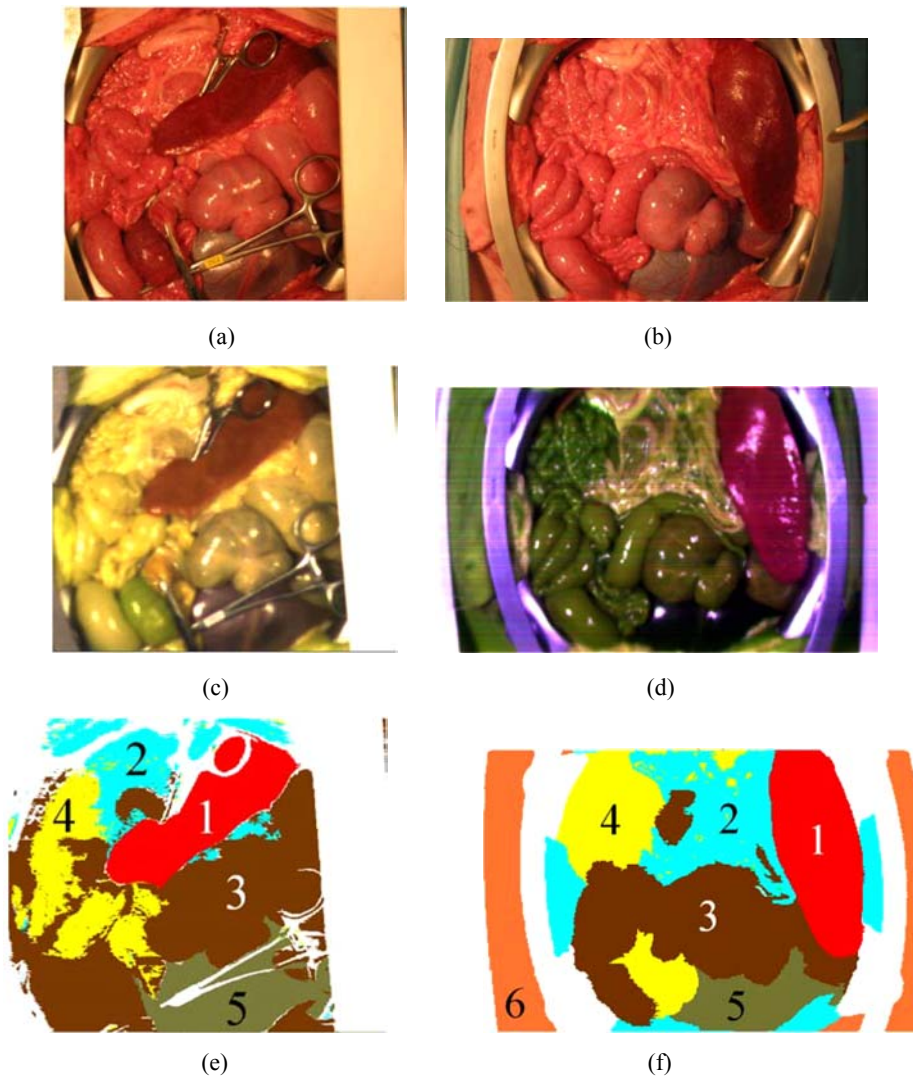


Table 1 The evaluation results and comparison with previously reported results

Camera	Organs	Spleen (%)	Urinary bladder (%)	Peritoneum (%)	Colon (%)	Small intestine (%)
V10E	FPR	3.9	3.7	5.3	5.1	8.7
	FNR	4.5	5.6	7.3	6.4	7.2
N17E	FPR	1.1	1.2	4.3	1.2	7.3
	FNR	1.3	0.7	5.1	9.5	2.7
N17E (previously reported)	FPR	0.5	1.3	6.3	1.2	12.3
	FNR	1.3	1.4	7.1	15	2.7

Source: Akbari et al. (2008a)

4 Discussion

The hyperspectral camera has entered the medical field as a new imaging modality. Using this high-tech instrument, the physician's vision is extended to invisible wavelengths. This technology expands the vision from the three RGB spectral bands to more than a 100 spectral bands. The large number of data in HSIs can be processed to broaden the spectral range and can supply useful information for surgeons. This previously invisible information can be accurately analysed and visualised for physician's use.

The spectral reflectance for each organ or tissue change is based on its characteristics. The peritoneum shows the highest value in visible, near-infrared and infrared wavelengths. One possible explanation could be the higher fat content of this tissue. In most spectral regions, the colon has the second highest reflectance value, after the peritoneum. In the colon, the adventitia forms small pouches filled with fatty tissue along the colon. The adventitia is the outermost layer of the Gastrointestinal (GI) tract that can be seen in the field of surgery. The muscularis externa is the layer deeper than adventitia in the GI tract, and its appearance is different from that of the small intestine. The outer longitudinal muscle of the colon forms three threads. Only a thin layer of muscle surrounds the inner circular muscle layer between these threads. These differences may result in different spectral reflectances. The urinary bladder is a hollow organ that consists of four layers. The mucous membrane, submucosa and the muscularis are the three inner layers. The outer layer is composed of fibrous connective tissue, which exists in all regions except the superior surface (Junqueira and Carneiro, 2005). This special histology and the fact that the urinary bladder is hollow inside can explain the lowest spectral reflectance measured for this organ. The spleen is the largest lymphoid organ, which is very rich in blood cells, and can act as a blood reservoir. This organ is covered by a firm fibrous capsule that maintains the external shape. The fibrous capsule of the spleen contains collagen, elastic fibres and smooth muscle (Junqueira and Carneiro, 2005). The spectral reflectance of the spleen has a different pattern compared with the other organs, which could be due to its unique histology. Between 450–650 nm and 800–1000 nm, it has the lowest reflectance value. However, the reflectance value rises from 1000 nm and ranks second in the wavelengths higher than 1200 nm.

Among different artificial neural network methods and machine classifiers, SVMs can successfully deal with high-dimensional data. Therefore, the data can be processed without compression. Even noisy data can be processed by an SVM. Compared with previous reports (Akbari et al., 2008a) where an LVQ was used to classify the HSIs, this paper shows superior results. According to the FPRs and the FNRs that are shown in Table 1, the N17E hyperspectral camera that captures infrared wavelengths is better for organ segmentation.

5 Conclusions

Hyperspectral imaging offers a valuable non-invasive tool for physicians or surgeons to assess and inspect a large area without actually removing tissue. Moreover, the extension of the surgeon's vision would be a significant breakthrough. An advantage of this technique is the capability to both spatially and spectrally verify the variations among different tissues or organs during surgery. The artificial neural network, the SVM algorithm, can incorporate detailed classification procedures that could be used for the region extraction and identification of organs or tissues.

Additionally, the spectral signatures of the spleen, colon, small intestine, peritoneum and urinary bladder are presented and can be used to identify these organs or tissues. This method could be useful in surgeries because it is important to be mindful of anatomical variations, tissue abnormalities and ectopic tissues. It would also enable a surgeon to be more vigilant during the surgery if he or she notices that there may be an abnormality or a normal variation in a particular region. This method enables continuous evaluation of the tissues without interrupting the surgery. In contrast, the previously implemented methods require the surgeon's attention to a special region and to use an instrument to extract a biopsy to send to a pathologist, which is a time-consuming method. Using this technique in surgeries will offer a novel exploration of pathology and may offer a new tool for early tumour detection.

References

- Aikio, M. (2001) *Hyperspectral Prism-Grating-Prism Imaging Spectrograph*, Espoo, Technical Research Centre of Finland, VTT Publications, Finland.
- Akbari, H., Kosugi, Y., Kojima, K. and Tanaka, N. (2008a) 'Wavelet-based compression and segmentation of hyperspectral images in surgery', *Springer Lecture Notes in Computer Science (LNCS)*, Vol. 5125, pp.142–149.
- Akbari, H., Kosugi, Y., Kojima, K. and Tanaka, N. (2008b) 'Hyperspectral imaging and diagnosis of intestinal ischemia', *Proceedings of the 30th Annual International Conference of the IEEE Engineering in Medicine and Biology Society*, August, Canada, pp.1238–1241.
- Bao, Y. and Liu, Z. (2006) 'A fast grid search method in support vector regression forecasting time series', *Lecture Notes in Computer Science (LNCS)*, Vol. 4224, pp.504–511.
- Brown, M., Lewis, H.G. and Gunn, S.R. (2000) 'Linear spectral mixture models and support vector machines for remote sensing', *IEEE Trans. Geosci. Remote Sens.*, Vol. 38, No. 5, pp.2346–2360.
- Camps-Valls, G. and Bruzzone, L. (2005) 'Kernel-based methods for hyperspectral image classification', *IEEE Trans. Geosci. Remote Sens.*, Vol. 43, pp.1351–1362.

- Camps-Valls, G., Gomez-Chova, L., Calpe-Maravilla, J., Martin-Guerrero, J.D., Soria-Olivas, E., Alonso-Chorda, L. and Moreno, J. (2004) 'Robust support vector method for hyperspectral data classification and knowledge discovery', *IEEE Trans. Geosci. Remote Sens.*, Vol. 42, No. 7, pp.1530–1542.
- Cancio, L.C., Batchinsky, A.I., Mansfield, J.R., Panasyuk, S., Hetz, K., Martini, D., Jordan, B.S., Tracey, B. and Freeman, J.E. (2006) 'Hyperspectral imaging: a new approach to the diagnosis of hemorrhagic shock', *J. Trauma-Injury Infect. Crit. Care*, Vol. 60, No. 5, pp.1087–1095.
- Datt, B., McVicar, T.R., van Niel, T.G., Jupp, D.L.B. and Pearlman, J.S. (2003) 'Preprocessing EO-1 hyperion hyperspectral data to support the application of agricultural indexes', *IEEE Trans. Geosci. Remote Sens.*, Vol. 41, pp.1246–1259.
- Freeman, J.E., Panasyuk, S., Rogers, A.E., Yang, S. and Lew, R. (2005) 'Advantages of intraoperative medical hyperspectral imaging (MHSI) for the evaluation of the breast cancer resection bed for residual tumor', *J. Clin. Oncol.*, Vol. 23, No. 16S, Part I of II (June 1 Supplement), p.709.
- Friedland, S., Benaron, D., Coogan, S., Sze, D.Y. and Soetikno, R. (2007) 'Diagnosis of chronic mesenteric ischemia by visible light spectroscopy during endoscopy', *Gastrointestinal Endoscopy*, Vol. 65, No. 2, pp.294–300.
- Huang, C., Davis, L.S. and Townshend, J.R. (2002) 'An assessment of support vector machines for land cover classification', *Int. J. Remote Sens.*, Vol. 23, No. 4, pp.725–749.
- Hughes, G.E. (1968) 'On the mean accuracy of statistical pattern recognizers', *IEEE Trans. Inf. Theory*, Vol. 14, pp.55–63.
- Junqueira, L.C. and Carneiro, J. (2005) *Basic Histology: Text & Atlas*, McGraw-Hill Companies, USA.
- Kellicut, D.C., Weiswasser, J.M., Arora, S., Freeman, J.E., Lew, R.A., Shuman, C., Mansfield, J.R. and Sidawy, A.N. (2004) 'Emerging technology: hyperspectral imaging', *Perspectives in Vascular Surgery and Endovascular Therapy*, Vol. 16, No. 1, pp.53–57.
- Khaodhiar, L., Dinh, T., Schomacker, K.T., Panasyuk, S.V., Freeman, J.E., Lew, R., Vo, T., Panasyuk, A.A., Lima, C., Giurini, J.M., Lyons, T.E. and Veves, A. (2007) 'The use of medical hyperspectral technology to evaluate microcirculatory changes in diabetic foot ulcers and to predict clinical outcomes', *Diabetes Care*, Vol. 30, No. 4, pp.903–910.
- Kohonen, T. (1987) *Self-Organization and Associative Memory*, Springer, Berlin.
- Lindsley, E.H., Wachman, E.S. and Farkas, D.L. (2004) 'The hyperspectral imaging endoscope: a new tool for in vivo cancer detection', *Proceedings of the SPIE*, Vol. 5322, pp.75–82.
- Liu, Z., Yan, J., Zhang, D. and Li, Q. (2007) 'Automated tongue segmentation in hyperspectral images for medicine', *Appl. Optics*, Vol. 46, No. 34, pp. 8328–8334.
- Martin, M.E., Wabuyele, M.B., Chen, K., Kasili, P., Panjehpour, M., Phan, M., Overholt, B., Cunningham, G., Wilson, D., Denovo, R.C. and Vo-dinh, T. (2006) 'Development of an advanced hyperspectral imaging (HSI) system with applications for cancer detection', *Annals of Biomedical Engineering*, Vol. 34, No. 6, pp.1061–1068.
- Melgani, F. and Bruzzone, L. (2004) 'Classification of hyperspectral remote sensing images with support vector machines', *IEEE Trans. Geosci. Remote Sens.*, Vol. 42, No. 8, pp.1778–1790.
- Monteiro, S.T., Uto, K., Kosugi, Y., Kobayashi, N. and Watanabe, E. (2006) 'Optimization of infrared spectral manipulation for surgical visual aid', *Journal of Japan Society of Computer Aided Surgery*, Vol. 8, No. 1, pp.33–38.
- Moran, J.A., Mitchell, A.K., Goodmanson, G. and Stockburger, K.A. (2000) 'Differentiation among effects of nitrogen fertilization treatments on conifer seedlings by foliar reflectance: a comparison of methods', *Tree Physiol.*, Vol. 20, pp.1113–1120.
- Poss, J.A., Russell, W.B. and Grieve, C.M. (2006) 'Estimating yields of salt- and water-stressed forages with remote sensing in the, visible and near infrared', *J. Environ. Qual.*, Vol. 35, pp.1060–1071.
- Richardson, A.D., Duigan, S.P. and Berlyn, G.P. (2002) 'An evaluation of noninvasive methods to estimate foliar chlorophyll content', *New Phytol.*, Vol. 153, pp.185–194.

- Suykens, J.A.K. and Vandewalle, J. (1999) 'Least squares support vector machine classifiers', *Neural Processing Letters*, Vol. 9, pp.293–300.
- Van Gestel, T., Suykens, J.A.K., Baesens, B., Viaene, S., Vanthienen, J., Dedene, G., De Moor, B. and Vandewalle, J. (2004) 'Benchmarking least squares support vector machine classifiers', *Machine Learning*, Vol. 54, No. 1, pp.5–32.
- Vapnik, V.N. (1995) *The Nature of Statistical Learning Theory*, Springer-Verlag, Berlin.
- Zuzak, K.J., Naik, S.C., Alexandrakis, G., Hawkins, D., Behbehani, K. and Livingston, E.H. (2007) 'Characterization of a near-infrared laparoscopic hyperspectral imaging system for minimally invasive surgery', *Anal. Chem.*, Vol. 79, pp.4709–4715.